On-Chip mm-Wave Second-/Third-Order BPF and Balun With Wide Stopband and Low Radiation Loss Using SIDGS Resonators in 40-nm CMOS

Deshan Tang, *Graduate Student Member, IEEE*, and Xun Luo, *Senior Member, IEEE*

***Abstract*— In this article, two millimeter-wave substrate-integrated defected ground structure (SIDGS) resonators are proposed for filters and balun implementation. Such SIDGS resonators are composed of defected ground structure (DGS) with grounded shield and surrounding vias, which not only exhibit wide stopband with low radiation loss but also are flexible to integrate with active circuits. Using different coupling methods, second-/third-order bandpass filters (BPFs) and filtering balun are designed based on the proposed SIDGS resonators. The filters and balun are fabricated in a standard 40-nm complementary metal-oxide-semiconductor (CMOS) technology. The second-order filter is centered at 28 GHz with an insertion loss of the 2.7 dB and 3-dB FBW of 20.4%. Meanwhile, the stopband extends to 140 GHz with a rejection level of 30 dB. The third-order filter operates at 28 GHz with an insertion loss of the 2.9 dB and 3-dB FBW of 47%. Meanwhile, the stopband extends to 170 GHz with a rejection level of 27 dB. The filtering balun operating at 25 GHz with the 3-dB FBW of 32% exhibits in-band amplitude/phase imbalances of 0.6 dB and ±1.1°, respectively. The minimum in-band insertion loss is 2 dB excluding the theoretical 3-dB loss. The stopband extends to 175 GHz with a rejection level of 30 dB.**

***Index Terms*— Bandpass filter (BPF), complementary metal-oxide-semiconductor (CMOS), filtering balun, low radiation loss, millimeter-wave, on-chip, resonator, substrate-integrated defected ground structure (SIDGS), wide stopband.**

I. Introduction

With the rapid development of modern wireless systems, passive components operating at mm-wave play an important role in many RF transceivers' front-ends. Compared with the passive components implemented on printed circuit board (PCB), on-chip mm-wave passive components [1], [2] alone with active devices can improve the system integrity and the reliability by avoiding the usage of complex packaging techniques.

Among different on-chip mm-wave passive components, filter is the most widely used device. Various approaches are proposed to design on-chip filter. The classical microstrip-based approach is the most popular one [3], [4], [5], [6], [7], [8], [9], [10]. Although the low insertion loss can be achieved by this approach, the designed filters occupy a relatively large area. To reduce the size of the filter, coplanar waveguide (CPW) structures are used in [11], [12], [13], [14], [15], [16], and [17]. By combining CPW and slow wave structures together, the physical size of a bandpass filter (BPF) can be reduced even more and additional transmission zero (TZ) can be introduced [16]. However, the stopband of the filters mentioned above is relatively narrow. To extend the stopband bandwidth, inverting-coupled inductors are used for filter design [18]. Nevertheless, such method suffers from the relatively large insertion loss and large radiation loss at stopband. On the other hand, most of the on-chip filters are mainly concentrated on first- or second-order BPF designs [3], [4], [5], [6], [7], [8], [9], [10], [11], [12], [13], [14], [15], [16], [17], [18], [19], [20], [21], which limit the passband bandwidth and passband selectivity. A third-order wideband BPF is proposed using broadside-coupled resonators [22], which exhibits relatively large insertion loss. Meanwhile, the design is only concentrated on passband, while the stopband performance is not easy to control. Therefore, on-chip mm-wave filter with a good in-band performance, wide stopband, high stopband rejection level, low radiation loss, good selectivity, and compact size remains a great challenge.

Balun is also an essential passive component in on-chip millimeter-wave circuits, which converts single-ended signals into balanced signals. Balanced signals improve the overall performance of circuits such as differential amplifiers, mixers, and frequency multipliers [23], [24], [25]. Marchand balun is widely used in on-chip balun due to its flexible implementation [26], [27], [28]. Coupled-CPW Marchand balun [29] is designed for large bandwidth, which suffers from the relatively large amplitude/phase imbalances and size. The size could be reduced by broadside-coupled spiral transmission line [30]. To further reduce amplitude and phase imbalances, the self-coupled compensation line is implemented in balun design [31]. To simplify the system design, filtering balun is proposed by integrating the function of filtering and balance-to-imbalance to one component. In [32] and [33], on-chip filtering baluns with good performance are designed for 5-GHz applications. To satisfy the application at mm-wave, a 24-GHz multicoupled line filtering balun is proposed [34]. However, such prototypes suffer from either relatively large phase imbalance or narrow stopband bandwidth. Therefore, the design of on-chip mm-wave filtering balun with good in-band performance, wide stopband, and compact size for flexible integration remains a great challenge.

Manuscript received 29 July 2022; accepted 15 November 2022. Date of publication 12 December 2022; date of current version 5 May 2023. This work was supported in part by the National Natural Science Foundation of China under Grant 62161160310 and Grant 61934001. *(Corresponding author: Xun Luo.)*

The authors are with the Center for Advanced Semiconductor and Integrated Micro-System, University of Electronic Science and Technology of China, Chengdu 611731, China (e-mail: xun-luo@ieee.org).

Color versions of one or more figures in this article are available at https://doi.org/10.1109/TMTT.2022.3226439.

Digital Object Identifier 10.1109/TMTT.2022.3226439

Recently, substrate-integrated defected ground structure (SIDGS) [35], [36], [37], [38], [39] is proposed for a series of high-performance passive components, which shows merits of wide stopband, low radiation loss, compact size, and low insertion loss. However, all these components are implemented on PCB, which is hard to integrate with active circuits directly.

In this article, two types of on-chip millimeter-wave SIDGS resonators are proposed, which are composed of defected ground structure (DGS) with grounded shield and surrounding vias. Such resonators not only exhibit wide stopband with low radiation loss but also are flexible to integrate with active circuits. Using different coupling methods combining with such SIDGS resonators, second-/third-order BPFs and filtering balun can be designed. Full simplified equivalent circuit models of the filters and balun are provided. By analyzing such models, guidelines for implementation of the filters and balun can be given. To verify the principle, the filters and balun are fabricated in a standard 40-nm complementary metal-oxide-semiconductor (CMOS) technology. The measured results exhibit merits of wide stopband with high rejection level, low radiation loss, low insertion loss, and good in-band amplitude/phase imbalances.

Compared with the SIDGS implemented on PCB technology in previous work [35], [36], [37], [38], [39], the SIDGS on the 40-nm CMOS in this work is a stacked structure with etched defects at different metal layers, while the previous work has only one layer of etched defect. Meanwhile, the complete bottom ground of SIDGS on PCB is replaced by the grounded shield in the design of SIDGS using the CMOS process. The reason for such a change is to satisfy the design rules of the 40-nm CMOS technology and avoid excessive parasitic capacitance. The CMOS-type SIDGS with the stacked structure can achieve a more compact size compared with the PCB-type SIDGS. Moreover, the on-chip SIDGS exhibits wider stopband bandwidth and lower radiation loss compared with other on-chip mm-wave structures and components. The article is organized as follows. In Section II, detailed analysis of the proposed two types of SIDGS resonators is presented. Section III demonstrates the implementation of the second-/third-order filters using the proposed SIDGS resonators and the analysis combining with the full simplified equivalent models. Then, Section VI presents theory and design example of the filtering balun. Finally, a brief conclusion is given in Section V.

II. On-Chip Millimeter-Wave SIDGS Resonators

The 3-D view of the proposed SIDGS resonators and the metal stack-up used for implementation are shown in Fig. 1. The metal stack-up is from a standard 40-nm CMOS technology. Resonator 1 consists of DGS located in M7 with the grounded shield in M6 and surrounding vias in V6. Resonator 2 consists of DGS located in M8 integrated with the grounded shield in M6 and surrounding vias in V6 and V7 connected by M7. Note that the physical size of these DGSs cannot meet the theoretical definition of slotline [40]. In SIDGS, the E-field and H-field of DGS can be confined by the grounded shield and surrounding vias, as illustrated in [35]. Thus, the loss of the resonators caused by the Si-substrate and radiation of the DGS can be minimized.

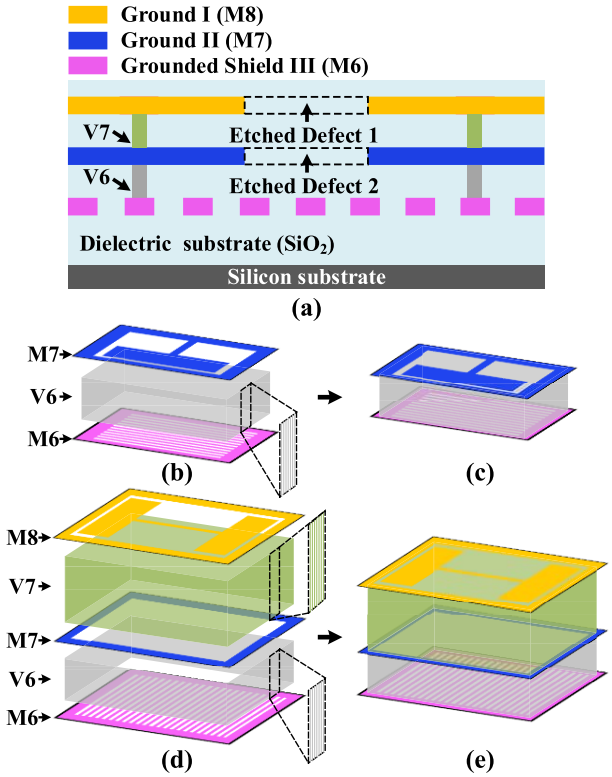

Fig. 1. (a) Cross-sectional view of the SIDGS in the 40-nm CMOS. (b) Metal stack-up and (c) 3-D view of the proposed SIDGS resonator 1. (d) Metal stack-up and (e) 3-D view of the proposed SIDGS resonator 2.

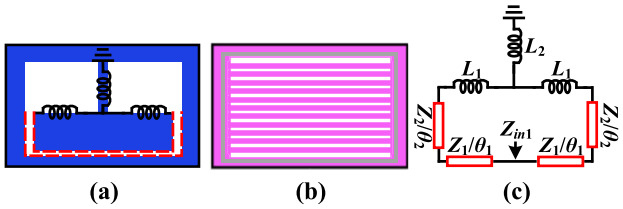

Fig. 2. Proposed SIDGS resonator 1. (a) Configuration of M7. (b) Configuration of V6 and M6. (c) Equivalent circuit.

To further illustrate the characteristic of the resonators, the simplified equivalent models based on the transmission lines and inductors are given. Fig. 2 shows the configuration and equivalent circuit of SIDGS resonator 1. The electrical length and characteristic impedance of the transmission line and the inductance could be extracted from the layout by full-wave simulation [41], [42]. Then, the input impedance of the resonator (i.e., Z_{in1}) is derived as (1), shown at the bottom of the page. The simulated and calculated input

$$Z_{\text{in1}} = \frac{Z_1}{2}\frac{j\omega Z_2(L_1+2L_2) + jZ_2^2\tan\theta_2 + jZ_1Z_2\tan\theta_1 - jZ_1\omega(L_1+2L_2)\tan\theta_1\tan\theta_2}{Z_1Z_2 - Z_1\omega(L_1+2L_2)\tan\theta_2 - \omega Z_2(L_1+2L_2)\tan\theta_1 - Z_2^2\tan\theta_1\tan\theta_2} \tag{1}$$

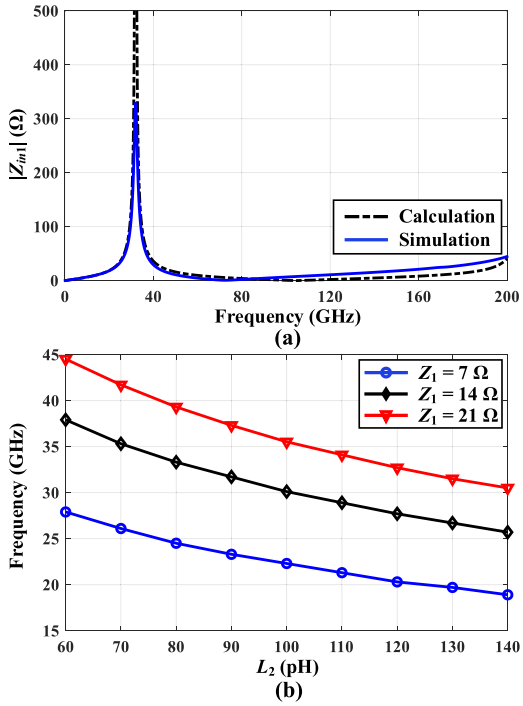

Fig. 3. (a) Calculated and simulated input impedances of SIDGS resonator 1. (b) Fundamental resonant frequency of the resonator under different characteristic impedances and inductances.

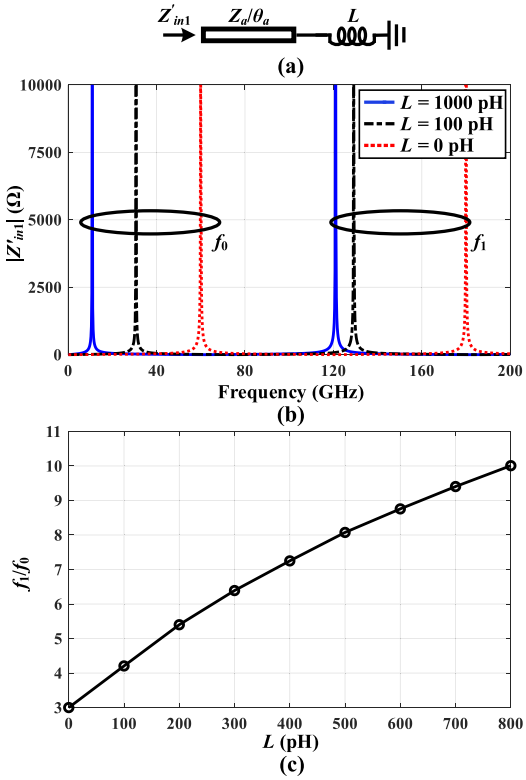

Fig. 4. (a) Simplified inductor-loaded resonator. (b) Calculated input impedance of the inductor-loaded resonator under different inductances. (c) Calculated ratio of the first spurious resonant frequency to the fundamental one with various loading inductances.

impedances are shown in Fig. 3(a), which show a good agreement. Meanwhile, the simulated unloaded quality factor Q_u is 22.3. The resonant frequency of the resonator can be tuned by characteristic impedance of the transmission line and the inductance of the inductor, as shown in Fig. 3(b). Meanwhile, such resonator exhibits an ultrawide stopband. To illustrate harmonic shifting, a simplified inductor-loaded transmission line will be discussed, as shown in Fig. 4(a). The input impedance is derived as

$$Z'_{\text{in1}} = Z_a \frac{j\omega L + jZ_a \tan\theta_a}{Z_a - \omega L \tan\theta_a}. \tag{2}$$

To further investigate the characteristic of the resonator, Z'_{in1} can be rewritten as

$$Z'_{\text{in1}} = jZ_a \frac{\tan\theta_a + \frac{\omega L}{Z_a}}{1 - \frac{\omega L}{Z_a}\tan\theta_a}. \tag{3}$$

Assume that

$$\tan\alpha = \frac{\omega L}{Z_a}\left(0 < \alpha < \frac{\pi}{2}\right). \tag{4}$$

Z'_{in1} can be rewritten as

$$Z'_{\text{in1}} = jZ_a \frac{\tan\theta_a + \tan\alpha}{1 - \tan\alpha\tan\theta_a} = jZ_a \tan(\theta_a + \alpha). \tag{5}$$

Note that the electrical length of the transmission line is affected by α, which is related to L. The equivalent electrical length (i.e., θ_d) and the equivalent phase velocity (i.e., v_{pd}) of the inductor-loaded transmission line can be derived as [43]

$$\frac{\omega l}{v_{pd}} = \theta_d = \theta_a + \alpha = \frac{\omega l}{v_{p0}} + \arctan\frac{\omega L}{Z_a} \tag{6}$$

$$v_{pd} = \frac{v_{p0}}{1 + \frac{v_{p0}\arctan\frac{\omega L}{Z_a}}{\omega l}} < v_{p0} \tag{7}$$

where v_{p0} is the phase velocity of the transmission line without loaded inductor, and l is the length of the transmission line. According to (7), a slow wave effect is achieved by the loaded inductor. With the loading inductance increasing, the slow wave effect is stronger. Fig. 4(b) shows plots of the input impedance of the inductor-loaded transmission line (Z_a = 20 Ω and $\theta_a = 90°$ at 60 GHz) under different inductance L. The resonance occurs when $|Z'_{\text{in1}}| = \infty$. Note that both fundamental resonant frequency (i.e., f_0) and spurious resonant frequency (i.e., f_1) decrease with the increase in L due to the slow wave effect. Combining (5) and (6), f_0 is obtained under the case of $\theta_d = \pi/2$ and f_1 is obtained under the case of $\theta_d = 3\pi/2$. Thus, $f_0 = \omega_0/2\pi = v_{pd0}/4l$ and $f_1 = \omega_0/2\pi = 3v_{pd1}/4l$, where v_{pd0} and v_{pd1} are the equivalent phase velocities of the inductor-loaded line at the fundamental and first spurious resonant frequencies, respectively. The ratio of f_1 to f_0 can be derived as

$$\frac{f_1}{f_0} = 3\frac{v_{pd1}}{v_{pd0}}. \tag{8}$$

According to (8), the slow wave effect can change the ratio of f_1 to f_0 by affecting the equivalent phase velocity v_{pd}. The calculated ratios of f_1 to f_0 for different loading inductances are presented in Fig. 4(c). It implies that with the loading inductance increasing, f_1/f_0 increases. Thus, the wide stopband could be achieved.

Fig. 5 shows the configuration and equivalent circuit of SIDGS resonator 2. Then, the input impedance of the resonator

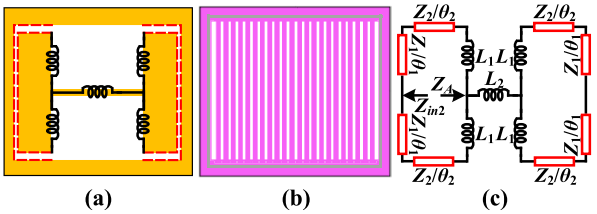

Fig. 5. Proposed SIDGS resonator 2. (a) Configuration of M8. (b) Configuration of V7 and M6. (c) Equivalent circuit.

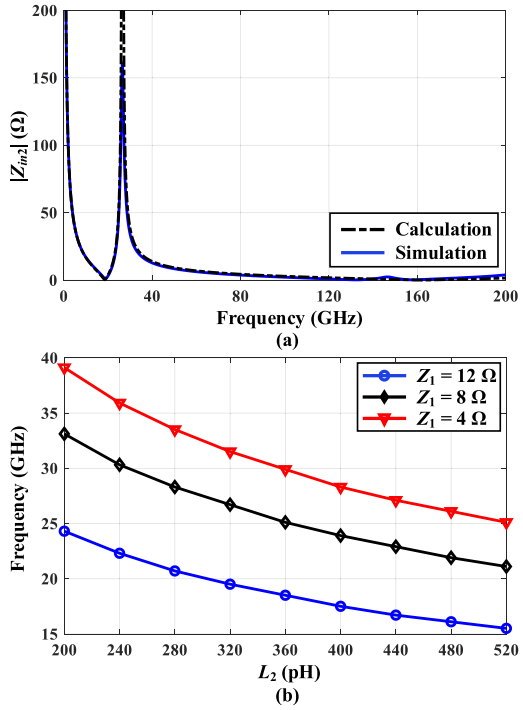

Fig. 6. (a) Calculated and simulated input impedances of SIDGS resonator 2. (b) Fundamental resonant frequency of the resonator under different characteristic impedances and inductances.

(i.e., Z_{in2}) is derived as (9), shown at the bottom of the page, where Z_A can be calculated as

$$Z_A = \frac{Z_2}{2}\frac{Z_1 - Z_2\tan\theta_1\tan\theta_2}{jZ_2\tan\theta_1 + jZ_1\tan\theta_2} + \frac{j\omega L_1}{2} + j\omega L_2. \quad (10)$$

The simulated and calculated input impedances are shown in Fig. 6(a). Meanwhile, the simulated unloaded quality factor Q_u is 21.4. The resonant frequency of the resonator can be tuned by different parameters, as shown in Fig. 6(b). The resonator also exhibits a characteristic of wide stopband. To illustrate harmonic shifting, a simplified inductor-connected transmission line will be discussed, as shown in Fig. 7(a). The even- and odd-mode circuits are shown in Fig. 7(b) and (c). The odd-mode circuit is similar to the simplified circuit in Fig. 4, which exhibits a slow wave effect affected by the loaded

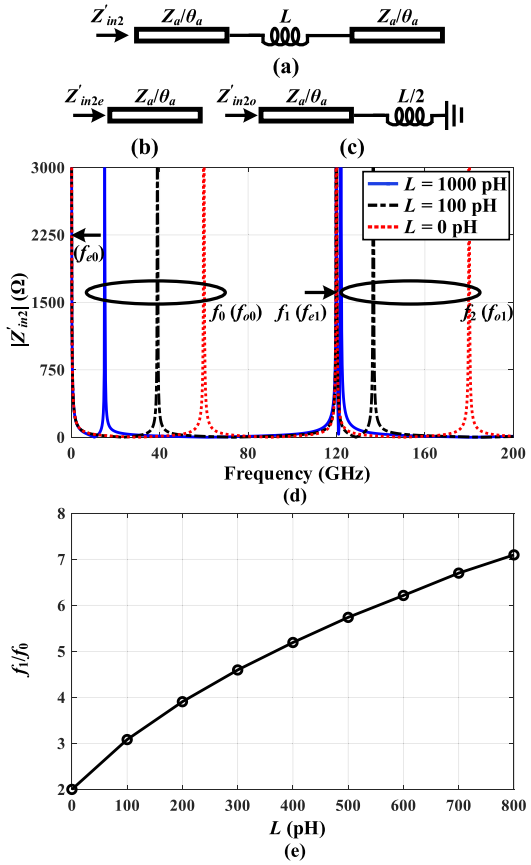

Fig. 7. (a) Simplified inductor-connected resonator. (b) Even-mode circuit. (c) Odd-mode circuit. (d) Calculated input impedance of the inductor-connected resonator under different inductances. (e) Calculated ratio of the spurious resonant frequency to the fundamental one with various connecting inductances.

inductor. The even-mode circuit is a typical half-wavelength resonator. The input impedances are derived as

$$Z'_{\text{in2e}} = \frac{Z_a}{j\tan\theta_a} \quad (11)$$

$$Z'_{\text{in2o}} = Z_a\frac{j\omega L + 2jZ_a\tan\theta_a}{2Z_a - \omega L\tan\theta_a} \quad (12)$$

$$Z'_{\text{in2}} = \frac{Z'_{\text{in2e}} + Z'_{\text{in2o}}}{2}. \quad (13)$$

Fig. 7(d) shows plots of the input impedance of the inductor-connected transmission line (Z_a = 20 Ω and θ_a = 90° at 60 GHz) under different inductance L. Note that the fundamental resonant frequency (i.e., f_0) of the inductor-connected transmission line is determined by the fundamental resonant frequency of the odd-mode circuit (i.e., f_{o0}). The first-harmonic resonant frequency of the inductor-connected transmission line (i.e., f_1) is determined by the fundamental resonant frequency of the even-mode circuit (i.e., f_{e1}). The second-harmonic resonant frequency of the

$$Z_{\text{in2}} = \frac{Z_1}{2}\frac{Z_2(j\omega L_1 + 2Z_A) + jZ_2^2\tan\theta_2 + jZ_1Z_2\tan\theta_1 - Z_1(j\omega L_1 + 2Z_A)\tan\theta_1\tan\theta_2}{Z_1Z_2 - Z_1(\omega L_1 - 2jZ_A)\tan\theta_2 - Z_2(\omega L_1 - 2jZ_A)\tan\theta_1 - Z_2^2\tan\theta_1\tan\theta_2} \quad (9)$$

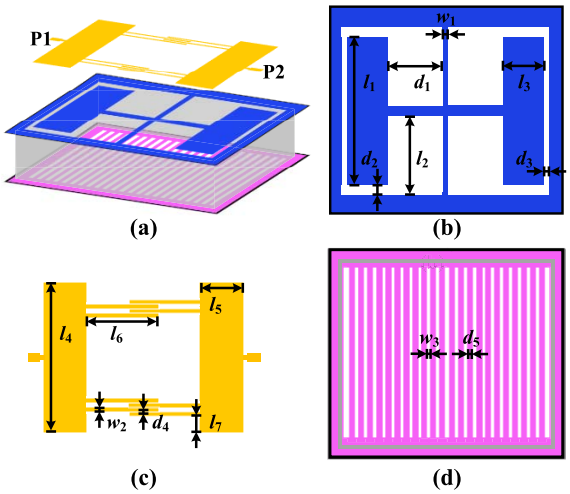

Fig. 8. (a) 3-D view of the second-order BPF. (b) Configuration of M7. (c) Configuration of M8. (d) Configuration of V6 and M6.

inductor-connected transmission line (i.e., f_2) is determined by the first-harmonic resonant frequency of the odd-mode circuit (i.e., f_{o1}). Thus, with the increase in L, f_0 and f_2 decrease while f_1 is fixed according to the characteristics of the even- and odd-mode circuits. Meanwhile, the calculated ratios of f_1 to f_0 for different inductance are presented in Fig. 7(e), which exhibits the ratio increasing with the inductance increasing. Thus, the wide stopband could be achieved.

III. Implementation and Analysis of BPF Using SIDGS Resonators

To prove that the proposed resonators are useful in practice, two on-chip second- and third-order BPF design examples are given. The full simplified equivalent circuits of the filters are provided for analyzing and assisting the design.

A. Implementation and Analysis of Second-Order BPF

To design a second-order BPF, two identical SIDGS resonator 1 are coupled to form a dual-resonance cell. Meanwhile, two T-stubs are used as the feed-line. The source-load coupling is achieved by interdigital capacitors connected to the feed-lines. The configuration and simplified equivalent circuit of the second-order BPF are shown in Figs. 8 and 9. To acquire the frequency response of the equivalent circuit, the even- and odd-mode analyses are used, as shown in Fig. 9(b) and (c). Using the Z-matrix of coupled line and transmission line impedance equation [43], the one-port input odd-mode admittance Z_{ino} can be derived as

$$Z_{\text{ino}} = \frac{Z_{11} - hZ_{13} - (k+g)Z_{14}}{2} \tag{14}$$

h, k, and g can be derived as

$$h = \frac{b(Z_{41} - gZ_{44}) - e(Z_{31} - gZ_{34})}{bd - ae} \tag{15}$$

$$k = \frac{d(Z_{31} - gZ_{34}) - a(Z_{41} - gZ_{44})}{bd - ae} \tag{16}$$

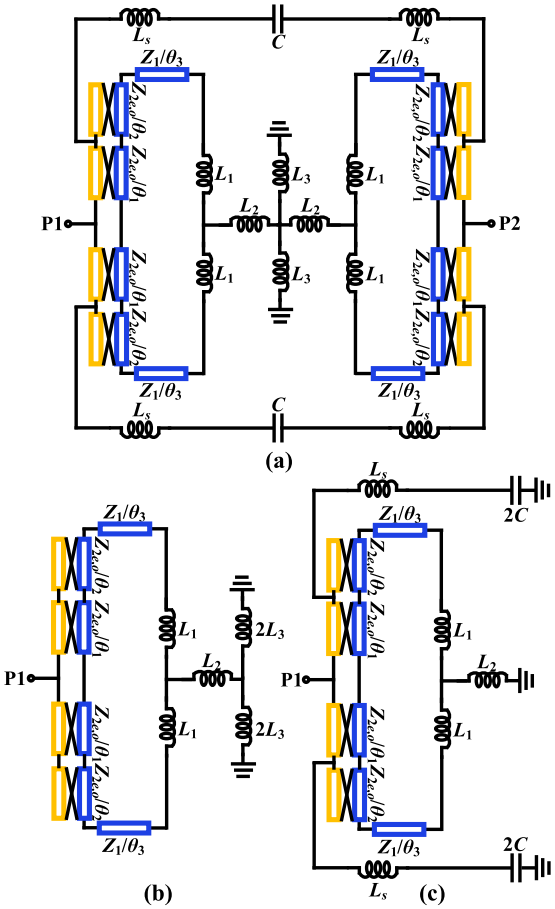

Fig. 9. (a) Equivalent circuit of the proposed second-order BPF. (b) Even-mode circuit. (c) Odd-mode circuit.

$$g = \frac{Z_{41} - Z_{43}\frac{bZ_{41} - eZ_{31}}{bd - ae} - Z_{44}\frac{dZ_{31} - aZ_{41}}{bd - ae}}{Z_x + Z_{44} - Z_{43}\frac{bZ_{44} - eZ_{34}}{bd - ae} - Z_{44}\frac{dZ_{34} - aZ_{44}}{bd - ae}} \tag{17}$$

a, b, d, e, and Z_x can be derived as

$$a = Z'_{11} + Z_{33} - \frac{Z'_{41}Z'_{14}}{Z_y + Z'_{44}} \tag{18}$$

$$b = Z'_{12} + Z_{34} - \frac{Z'_{41}Z'_{24}}{Z_y + Z'_{44}} \tag{19}$$

$$d = Z'_{21} + Z_{43} - \frac{Z'_{41}Z'_{12}}{Z_y + Z'_{44}} \tag{20}$$

$$e = Z'_{22} + Z_{44} - \frac{Z'_{21}Z'_{12}}{Z_y + Z'_{44}} \tag{21}$$

$$Z_x = j\omega L_s + \frac{1}{2j\omega C}. \tag{22}$$

Z_y can derived as

$$Z_y = Z_1\frac{j\omega(L_1 + 2L_2) + jZ_1\tan\theta_3}{Z_1 - \omega(L_1 + 2L_2)\tan\theta_3}. \tag{23}$$

The one-port input even-mode admittance Z_{ine} can be derived as

$$Z_{\text{ine}} = \frac{1}{2}\left(Z''_{11} - \frac{Z''_{13}Z''_{31}}{Z_m + Z''_{33}}\right). \tag{24}$$

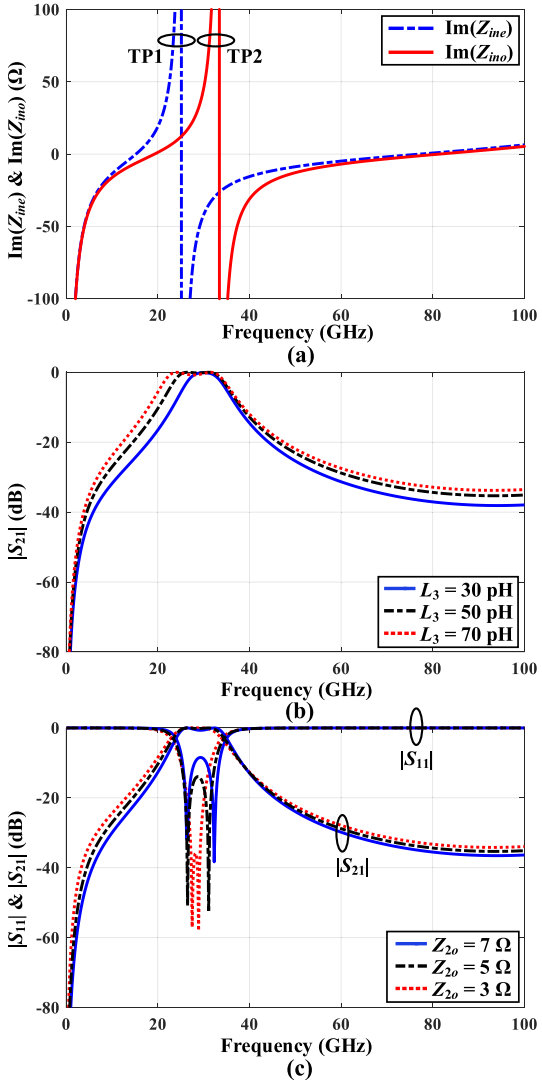

Fig. 10. (a) Calculated input impedances of even mode and odd mode when $C = 0$ fF. (b) Calculated $|S_{21}|$ under different L_3. (c) Calculated $|S_{11}|$ and $|S_{21}|$ under different Z_{2o}.

Z_m can be calculated as

$$Z_m = Z_1 \frac{j\omega(L_1 + 2L_2 + 2L_3) + jZ_1 \tan\theta_3}{Z_1 - \omega(L_1 + 2L_2 + 2L_3)\tan\theta_3} \tag{25}$$

Z_{ij}, Z'_{ij}, and Z''_{ij} $(i, j = 1, 2, 3, 4)$ are the Z-matrix parameters of coupled line, which are derived in Appendix. Therefore, the S-parameters of the proposed circuit shown in Fig. 9(a) can be expressed as

$$S_{11} = S_{22} = \frac{Z_{\text{ine}} Z_{\text{ino}} - Z_0^2}{(Z_0 + Z_{\text{ino}})(Z_0 + Z_{\text{ine}})} \tag{26}$$

$$S_{21} = S_{12} = \frac{Z_0(Z_{\text{ine}} - Z_{\text{ino}})}{(Z_0 + Z_{\text{ino}})(Z_0 + Z_{\text{ine}})} \tag{27}$$

where $Z_0 = 50\ \Omega$.

The calculated results of various cases are given in Figs. 10 and 11. To clarify the order, the calculated even- and odd-mode impedances under the case of $C = 0$ fF are shown in Fig. 10(a). Two transmission poles (TPs) are generated by even- and odd-mode circuits, which implies that the BPF

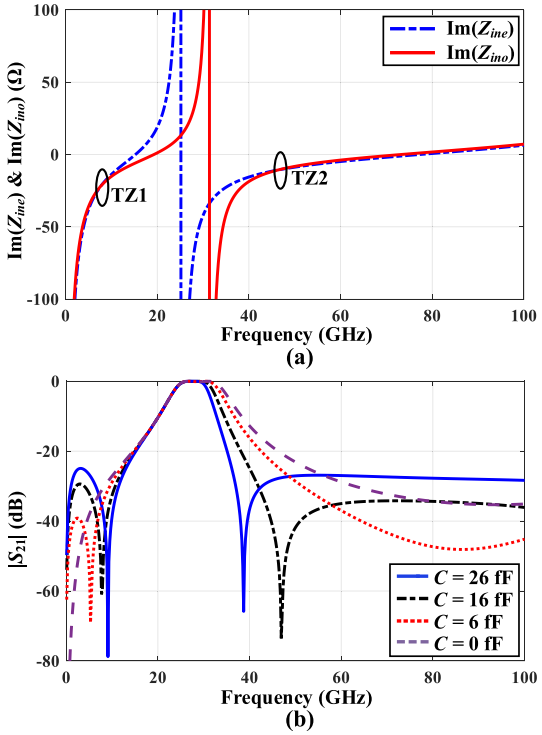

Fig. 11. (a) Calculated input impedances of even mode and odd mode when $C = 16$ fF. (b) Calculated $|S_{21}|$ under different C.

is second-order. The center frequency of the second-order BPF is mainly determined by the parameters of resonators, as mentioned in Section II. Note that two resonators are coupled by two additional inductors L_3, as shown in Fig. 9. Thus, the bandwidth of the second-order BPF can be tuned by changing L_3. Fig. 10(b) shows the S-parameter under different L_3. The bandwidth of the filter increases with the increase in L_3. After the bandwidth is determined, the loading strength of the feed-line can be adjusted by Z_{2o} of the coupled line. Fig. 10(c) shows the S-parameter under different Z_{2o}. Suitable loading strength of the feed-line could be found by tuning Z_{2o}.

To enhance the passband selectivity and stopband rejection level, additional TZs should be generated. According to (27), the TZs could be generated under the condition of $Z_{\text{ine}} = Z_{\text{ino}}$. In this design, the TZs could be generated by changing the odd-mode impedance using source-load coupling capacitor C. Fig. 11(a) shows Z_{ino} and Z_{ine} under $C = 16$ fF. Compared with Fig. 10(a), the curves of the even- and odd-mode impedances intersect at the positions of TZ1 and TZ2. Fig. 11(b) shows the calculated S-parameter under different capacitance C. With the increase in C, the TZs are closer to the passband. The calculated and simulated S-parameters of the proposed second-order BPF are shown in Fig. 12(a), which shows a good agreement. Besides, radiation/conductor/dielectric loss rates of the second-order BPF are simulated and calculated, as shown in Fig. 12(b). The radiation loss is simulated under the case of lossless metal and substrate (i.e., S_{11r}, S_{21r}). The radiation loss L_r is calculated as

$$L_r = 1 - |S_{11r}|^2 - |S_{21r}|^2. \tag{28}$$

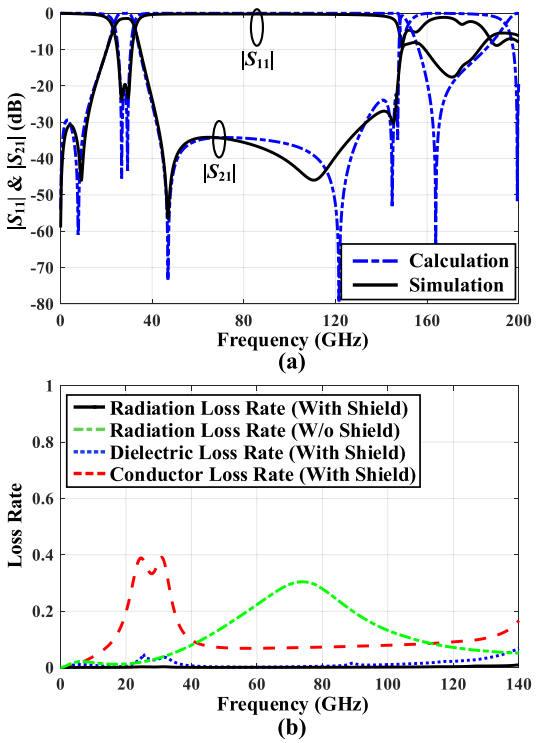

Fig. 12. (a) Calculated and simulated $|S_{11}|$ and $|S_{21}|$ of the second-order BPF. (b) Simulated radiation/conductor/dielectric loss rates of the second-order BPF ($l_1 = 199.8$, $l_2 = 99$, $l_3 = 38.7$, $l_4 = 199.8$, $l_5 = 37.8$, $l_6 = 85.05$, $l_7 = 26.1$, $d_1 = 61.2$, $d_2 = 5.4$, $d_3 = 3.6$, $d_4 = 1.8$, $d_5 = 3.6$, $w_1 = 10.8$, $w_2 = 3.6$, and $w_3 = 3.6$, unit: μm. $C = 17$ fF, $L_1 = 18$ pH, $L_2 = 41$ pH, $L_3 = 53$ pH, $L_s = 15$ pH, $Z_1 = 55\ \Omega$, $Z_{2e} = 39\ \Omega$, $Z_{2o} = 5\ \Omega$, $\theta_1 = 16.1°$, $\theta_2 = 18.4°$, and $\theta_3 = 2.8°$).

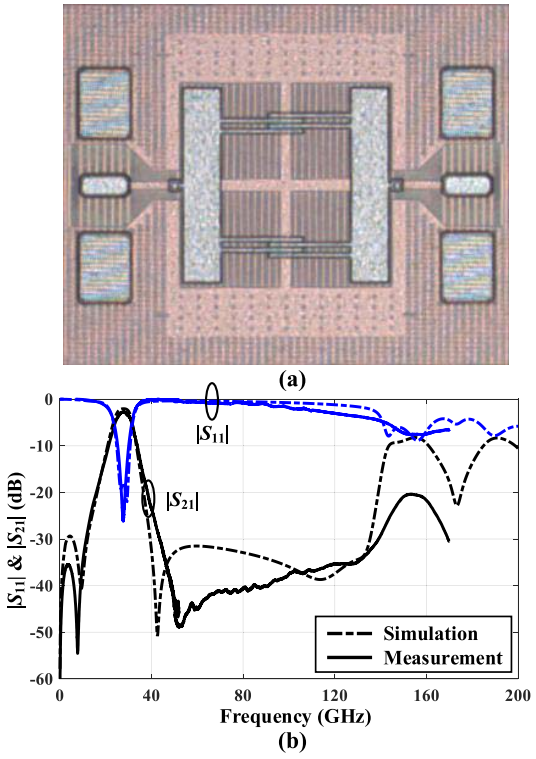

Fig. 13. (a) Photograph of the proposed second-order BPF. (b) Measured and simulated results of the proposed second-order BPF.

The conductor loss L_c and dielectric loss L_d can be calculated under the cases of lossless dielectric (i.e., S_{11c}, S_{21c}) or lossless metal (i.e., S_{11d}, S_{21d}), respectively. L_c and L_d can be derived as

$$L_{c,d} = 1 - |S_{11c,d}|^2 - |S_{21c,d}|^2 - L_r. \tag{29}$$

The design procedure of the second-order BPF is summarized as follows. The first step is to obtain the parameters of the resonators according to the center frequency of the filter specifications. Note that the center frequency of the filter mainly depends on the resonant frequency of the resonators. According to Figs. 3(b) and 6(b), the specific parameters of resonators under different resonant frequencies can be obtained. The second step is to obtain the parameters about coupling relationship of the resonators and feed-line according to the specification of bandwidth and TZ. The desired bandwidth can be obtained by adjusting the value of coupling inductor L_3, as shown in Fig. 10(b). After L_3 is determined, the suitable loading strength of feed-line can be obtained by adjusting the value of Z_{2o}, according to Fig. 10(c). Then, the desired location of TZ can be obtained by adjusting the value of source-load coupling capacitor C, according to Fig. 11(b). The third step is to implement the layout of the filters according to the parameters of the equivalent circuits.

Based on the design procedure mentioned above, the second-order BPF is fabricated in a standard 40-nm CMOS technology, as displayed in Fig. 13(a). The pitch between the ground pad to the signal pad is 85 μm. The feed-line is 50 Ω CPW. The thru–reflect–line (TRL) calibration is used for measurement. The measurement is calibrated to the tips of probes. Thus, the measured result is including the influence of ground-signal-ground (GSG) pad and feed-lines. The simulated and measured results of the S-parameters are shown in Fig. 13(b). The vector network analyzer is used to measure. The center frequency of the BPF is 28 GHz with the 3-dB FBW of 20.4%. The minimum in-band insertion loss is 2.7 dB. Meanwhile, the stopband is up to 140 GHz with a rejection level higher than 30 dB. The stopband $|S_{11}|$ is higher than -4 dB up to 140 GHz, which implies that the BPF exhibits a low radiation loss within a wide frequency range using SIDGS. In addition, the core circuit size of the BPF is 225 $\times$ 225 μm^2.

B. Implementation and Analysis of Third-Order BPF

To design a wideband third-order BPF, three stacked-coupled SIDGS resonators 1 and 2 are used. Such stacked-coupled scheme can reduce the size of the filter. The feed-lines are tapped to two resonator 2. Meanwhile, the cross coupling of two resonator 2 is introduced by the parallel-plate capacitor. The configuration and simplified equivalent circuit of the third-order BPF are shown in Figs. 14 and 15, respectively. To demonstrate the mechanism, the equivalent circuit should be analyzed first using even- and odd-mode circuits, as shown in Fig. 15(b) and (c), respectively. To acquire the frequency response of the circuit, the one-port input even- and odd-mode impedances Y_{ine} and Y_{ino} can be derived as [43] and [44]

$$Y_{\text{ine}} = Y_{11}^a - \frac{Y_{12}^a Y_{21}^a}{\frac{1}{j\omega L_{2e}} + Y_{22}^a} = Y_{11}^a - \frac{Y_{12}^a Y_{21}^a}{\frac{1}{j\omega L_2(1+k_2)} + Y_{22}^a} \tag{30}$$

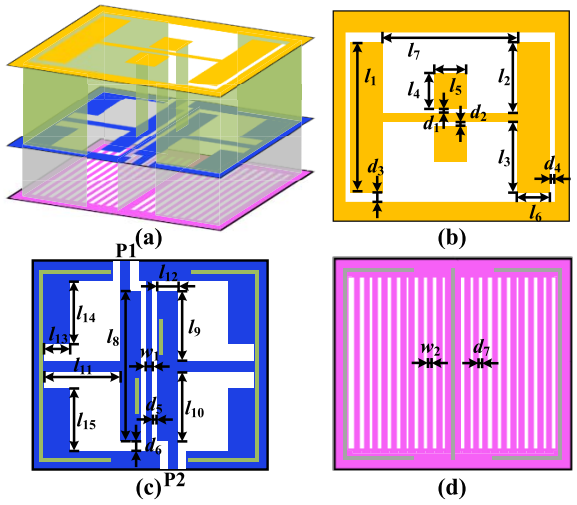

Fig. 14. (a) 3-D view of the third-order BPF. (b) Configuration of M8. (c) Configuration of V7 and M7. (d) Configuration of V6 and M6.

$$Y_{\text{ino}} = Y_{11}^b - \frac{Y_{12}^b Y_{21}^b}{Y_m + Y_{22}^b}. \tag{31}$$

Y_m is calculated as

$$\frac{1}{Y_m} = Z_m = j\omega(L_{2o} - M) + \frac{j\omega M(j\omega(L_3 - M) + Z_n)}{j\omega L_3 + Z_n}. \tag{32}$$

L_{2o}, M, and Z_n are derived as

$$L_{2o} = (1 - k_2)L_2 \tag{33}$$

$$M = k_{1o}\sqrt{L_{2o}L_3} = k_1\sqrt{L_2/L_{2o}}\sqrt{L_{2o}L_3} \tag{34}$$

$$\frac{1}{Z_n} = Y_n = Y_{11}^c - \frac{Y_{12}^c Y_{21}^c}{Y_{22}^c}. \tag{35}$$

Y_{11}^x, Y_{12}^x, Y_{21}^x, and Y_{22}^x $(x = a, b, c)$ are calculated as

$$Y_{11}^x = \frac{D_1^x}{B_1^x} + \frac{D_2^x}{B_2^x} \tag{36}$$

$$Y_{12}^x = \frac{B_1^x C_1^x - A_1^x D_1^x}{B_1^x} + \frac{B_2^x C_2^x - A_2^x D_2^x}{B_2^x} \tag{37}$$

$$Y_{21}^x = \frac{-1}{B_1^x} + \frac{-1}{B_2^x} \tag{38}$$

$$Y_{22}^x = \frac{A_1^x}{B_1^x} + \frac{A_2^x}{B_2^x} \tag{39}$$

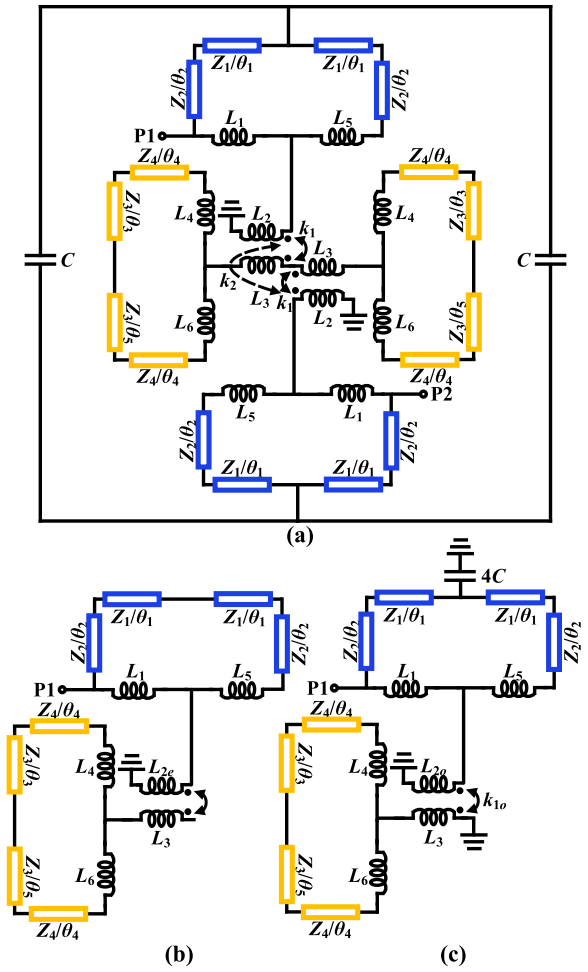

Fig. 15. (a) Equivalent circuit of the proposed third-order BPF. (b) Even-mode circuit. (c) Odd-mode circuit.

where $A_{1,2}^x$, $B_{1,2}^x$, $C_{1,2}^x$, and $D_{1,2}^x$ $(x = a, b, c)$ are derived in (40)–(43), as shown at the bottom of the page.

$$\begin{pmatrix} A_2^a & B_2^a \\ C_2^a & D_2^a \end{pmatrix} = \begin{pmatrix} A_2^b & B_2^b \\ C_2^b & D_2^b \end{pmatrix} = \begin{pmatrix} 1 & j\omega L_1 \\ 0 & 1 \end{pmatrix}. \tag{40}$$

Then, the S-parameters of proposed circuit shown in Fig. 15(a) can be calculated by (26) and (27). The calculated results of various cases are given in Figs. 16 and 17. To confirm the order of the BPF, C is set as 0 fF and k_2 is set as 0. The calculated even- and odd-mode impedances are shown in Fig. 16(a). Three TPs are generated by even- and odd-mode

$$\begin{pmatrix} A_1^a & B_1^a \\ C_1^a & D_1^a \end{pmatrix} = \begin{pmatrix} \cos\theta_2 & jZ_2\cos\theta_2 \\ jY_2\sin\theta_2 & \cos\theta_2 \end{pmatrix}\begin{pmatrix} \cos 2\theta_1 & jZ_1\cos 2\theta_1 \\ jY_1\sin 2\theta_1 & \cos 2\theta_1 \end{pmatrix}\begin{pmatrix} \cos\theta_2 & jZ_2\cos\theta_2 \\ jY_2\sin\theta_2 & \cos\theta_2 \end{pmatrix}\begin{pmatrix} 1 & j\omega L_5 \\ 0 & 1 \end{pmatrix} \tag{41}$$

$$\begin{pmatrix} A_1^b & B_1^b \\ C_1^b & D_1^b \end{pmatrix} = \begin{pmatrix} \cos\theta_2 & jZ_2\cos\theta_2 \\ jY_2\sin\theta_2 & \cos\theta_2 \end{pmatrix}\begin{pmatrix} \cos\theta_1 & jZ_1\cos\theta_1 \\ jY_1\sin\theta_1 & \cos\theta_1 \end{pmatrix}\begin{pmatrix} 1 & 0 \\ 4j\omega C & 1 \end{pmatrix} \times\begin{pmatrix} \cos\theta_1 & jZ_1\cos\theta_1 \\ jY_1\sin\theta_1 & \cos\theta_1 \end{pmatrix}\begin{pmatrix} \cos\theta_2 & jZ_2\cos\theta_2 \\ jY_2\sin\theta_2 & \cos\theta_2 \end{pmatrix}\begin{pmatrix} 1 & j\omega L_5 \\ 0 & 1 \end{pmatrix} \tag{42}$$

$$\begin{pmatrix} A_{1,2}^c & B_{1,2}^c \\ C_{1,2}^c & D_{1,2}^c \end{pmatrix} = \begin{pmatrix} 1 & j\omega L_{4,6} \\ 0 & 1 \end{pmatrix}\begin{pmatrix} \cos\theta_4 & jZ_4\cos\theta_4 \\ jY_4\sin\theta_4 & \cos\theta_4 \end{pmatrix}\begin{pmatrix} \cos\theta_{3,5} & jZ_3\cos\theta_{3,5} \\ jY_3\sin\theta_{3,5} & \cos\theta_{3,5} \end{pmatrix} \tag{43}$$

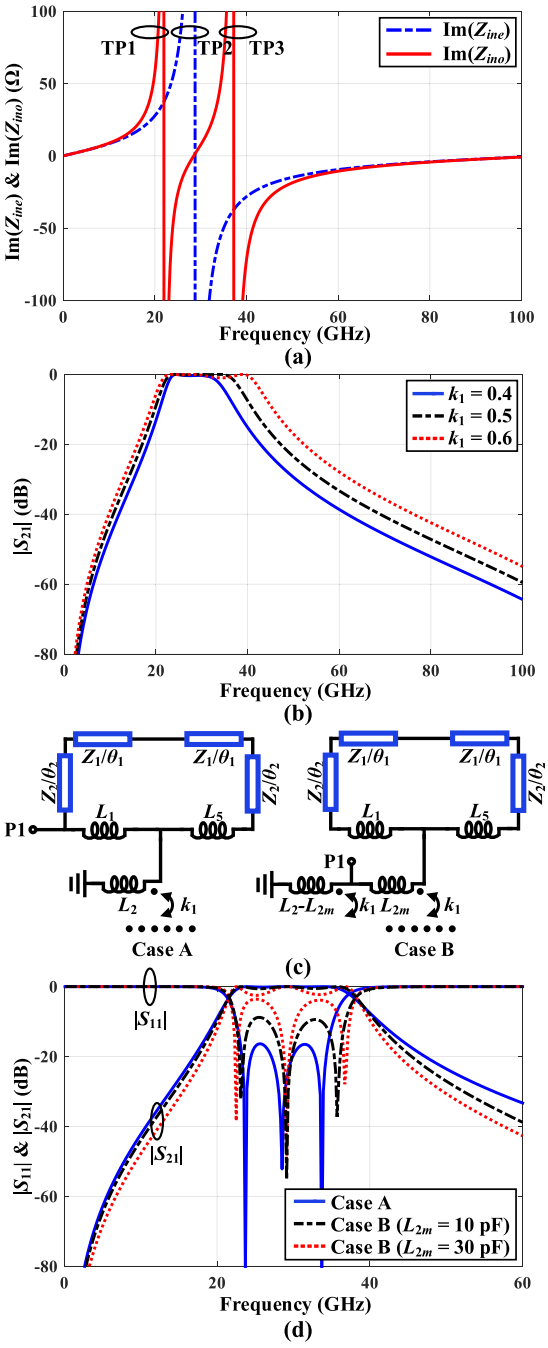

Fig. 16. (a) Calculated input impedances of even mode and odd mode when $C = 0$ fF and $k_2 = 0$. (b) Calculated $|S_{21}|$ under different k_1. (c) Different tapped positions of the feed-line (i.e., Cases A and B). (d) Calculated $|S_{21}|$ and $|S_{11}|$ under different tapped positions.

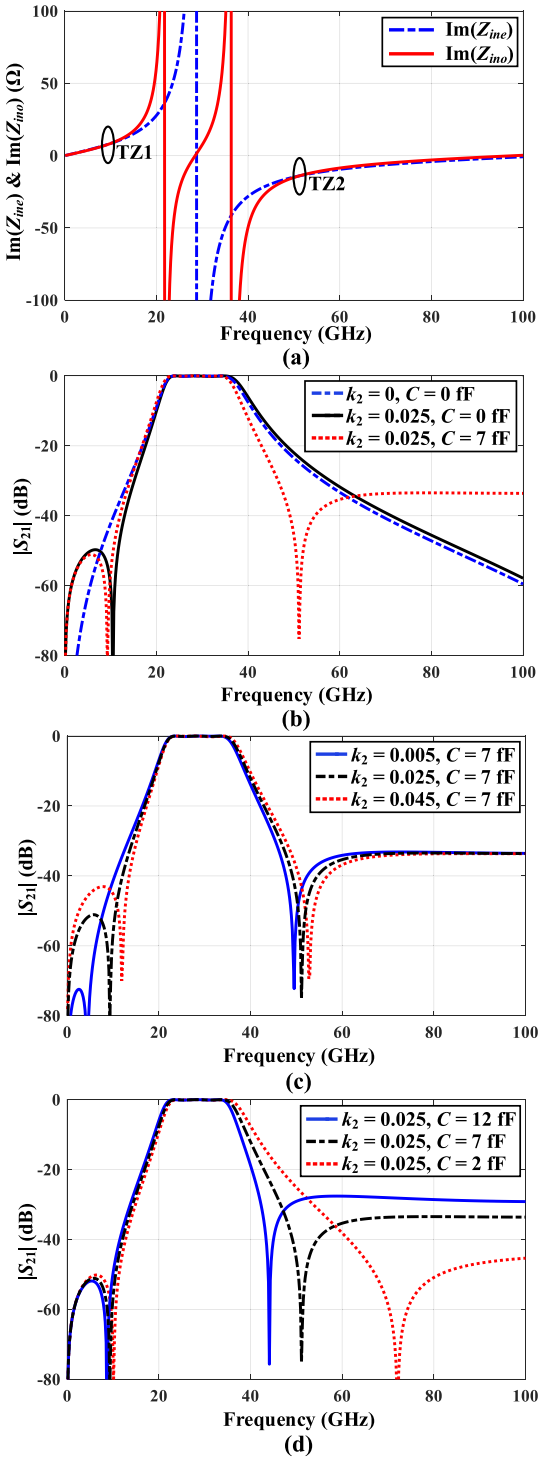

Fig. 17. (a) Calculated input impedances of even mode and odd mode when $C = 7$ fF and $k_2 = 0.025$. (b) Calculated $|S_{21}|$ under various C and k_2. (c) Calculated $|S_{21}|$ under different k_2 when $C = 7$ fF. (d) Calculated $|S_{21}|$ under different C when $k_2 = 0.025$.

circuits, which implies that the BPF is third-order. The center frequency of the third-order BPF is mainly determined by the parameters of two types of resonators mentioned in Section II. Note that three resonators are coupled by three inductive parts in series, as shown in Fig. 15(a). Thus, the bandwidth of the third-order BPF can be tuned by changing the coupling coefficient k_1, as shown in Fig. 16(b). Note that the feed-line is tapped to the filter. Fig. 16(c) depicts the schematic of different tapped positions of the feed-line (i.e., Cases A and B). By changing the tapped position, suitable loading strength of the feed-lines can be obtained for good passband performance, as shown in Fig. 16(d).

To enhance the passband selectivity and stopband rejection level, additional TZs can be generated at the upper and lower stopbands under the condition of $Z_{\text{ine}} = Z_{\text{ino}}$, as mentioned in Section III-A. In this design, two cross couplings including the magnetic coupling between the inductor L_2 of two resonator 1

TABLE I
COMPARISON OF STATE-OF-THE-ART ON-CHIP BPFS

Ref.	Technology & Structure	Filter Order	f_c (GHz)	Insertion Loss (dB)	FBW (%)	Stopband Rejection	Stopband $\lvert S_{11}\rvert$	Core Size
[7]	0.18-μm CMOS & MS	2	58.5	3.5	15.4	>20 dB up to 110 GHz ($1.9f_c$)	>-5 dB up to 110 GHz ($1.9f_c$)*	0.074 mm^2
[11]	0.18-μm CMOS & CPW	2	11.5	2.78	36.5	>20 dB up to 25 GHz ($2.2f_c$)	N/A	0.246 mm^2
[18]	0.13-μm SiGe & ICI	2	17	3.5	27.8	>30 dB up to 67 GHz ($3.9f_c$)	>-4 dB up to 67 GHz ($3.9f_c$)*	0.053 mm^2
[19]	0.13-μm (Bi)-CMOS & QLE	2	29	3.5	26.7	>20 dB up to 67 GHz ($2.3f_c$)	>-4 dB up to 67 GHz ($2.3f_c$)*	0.028 mm^2
[20]	0.13-μm (Bi)-CMOS & MPG	2	31	2.7	17.5	>30 dB up to 67 GHz ($2.2f_c$)	N/A	0.044 mm^2
[22]	0.13-μm (Bi)-CMOS & BCR	3	31	3.9	51	>20 dB up to 70 GHz ($2.2f_c$)	>-6 dB up to 70 GHz ($2.2f_c$)*	0.075 mm^2
This work I	**40-nm CMOS & SIDGS**	**2**	**28**	**2.7**	**20.4**	**>30 dB up to 140 GHz ($5f_c$)**	**>-4 dB up to 140 GHz ($5f_c$)**	**0.051 mm^2**
This work II	**40-nm CMOS & SIDGS**	**3**	**28**	**2.9**	**47**	**>27 dB up to 170 GHz ($6.1f_c$)**	**>-4 dB up to 155 GHz ($5.5f_c$)**	**0.073 mm^2**

*: Estimated from the figure.

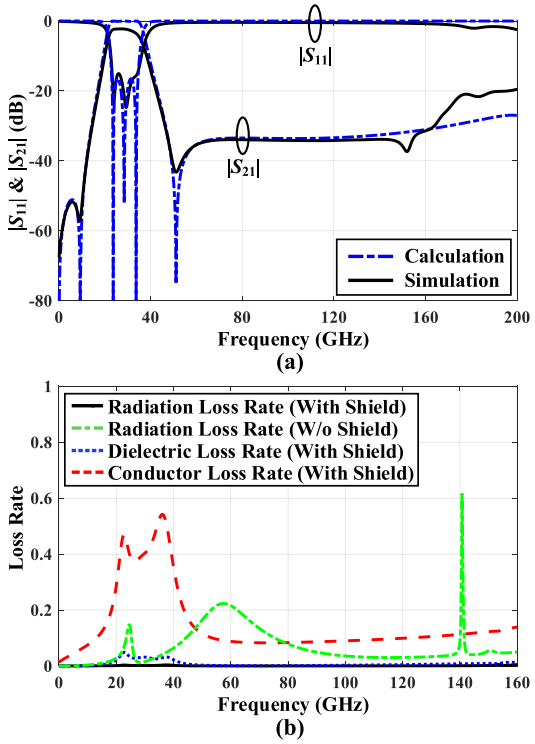

Fig. 18. (a) Calculated and simulated $|S_{11}|$ and $|S_{21}|$ of the third-order BPF. (b) Simulated radiation/conductor/dielectric loss rates of the third-order BPF ($l_1 = 228.6$, $l_2 = 93.15$, $l_3 = 129.15$, $l_4 = 24.3$, $l_5 = 27$, $l_6 = 33.3$, $l_7 = 194.4$, $l_8 = 228.6$, $l_9 = 130.5$, $l_{10} = 91.8$, $l_{11} = 109.62$, $l_{12} = 19.8$, $l_{13} = 35.1$, $l_{14} = 122.85$, $l_{15} = 84.15$, $d_1 = 15.3$, $d_2 = 51.3$, $d_3 = 5.4$, $d_4 = 1.8$, $d_5 = 1.8$, $d_6 = 5.4$, $d_7 = 3.6$, $w_1 = 2.16$, and $w_2 = 3.6$, unit: μm. $C = 7$ fF, $L_1 = 9$ pH, $L_2 = 109$ pH, $L_3 = 178$ pH, $L_4 = 18$ pH, $L_5 = 13$ pH, $L_6 = 24$ pH, $k_1 = 0.5$, $k_2 = 0.025$, $Z_1 = 14$ Ω, $Z_2 = 15$ Ω, $Z_3 = 8$ Ω, $Z_4 = 10$ Ω, $\theta_1 = 15.4°$, $\theta_2 = 2.7°$, $\theta_3 = 6°$, $\theta_4 = 1.5°$, and $\theta_5 = 8.6°$).

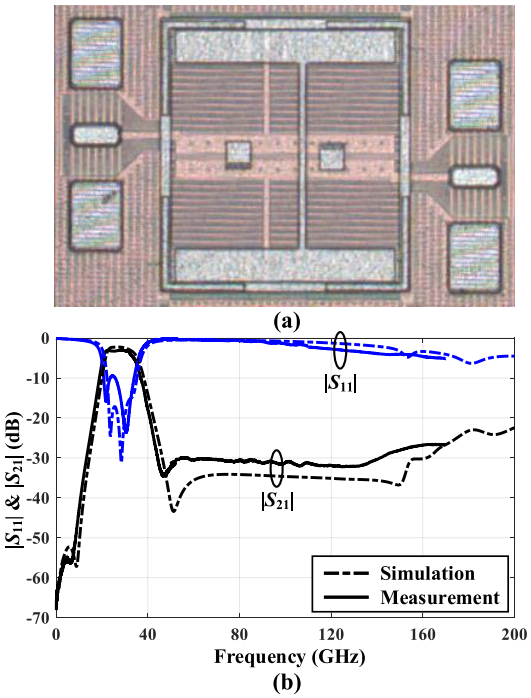

Fig. 19. (a) Photograph of the proposed third-order BPF. (b) Measured and simulated results of the proposed third-order BPF.

and the electric coupling caused by the parallel-plate capacitors can change Z_{ino}, as shown in Fig. 15. Fig. 17(a) shows Z_{ino} and Z_{ine} under $C = 7$ fF and $k_2 = 0.025$, which exhibits two additional intersects compared with Fig. 16(b). Fig. 17(b) demonstrates the S-parameters under different C and k_2. Note that the magnetic coupling between the inductors of two resonator 1 could generate a TZ at the lower stopband. Meanwhile, the electric coupling caused by the parallel-plate capacitors between two resonator 1 could generate a TZ at the upper stopband. In addition, two TZs can be independently adjusted by C and k_2, as shown in Fig. 17(c) and (d). The calculated and simulated S-parameters of the proposed third-order BPF are shown in Fig. 18(a), which shows a good agreement. Besides, radiation/conductor/dielectric loss rates of the third-order BPF are simulated and calculated, as shown in Fig. 18(b).

The design procedure of the third-order BPF is summarized as follows. The first step is to obtain the parameters of the

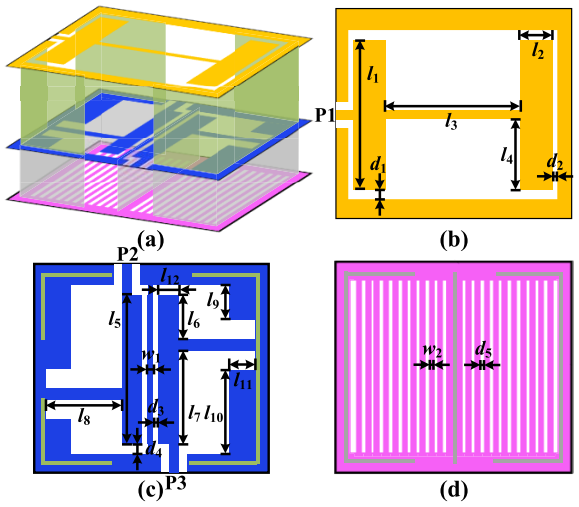

Fig. 20. (a) 3-D view of the filtering balun. (b) Configuration of M8. (c) Configuration of V7 and M7. (d) Configuration of V6 and M6.

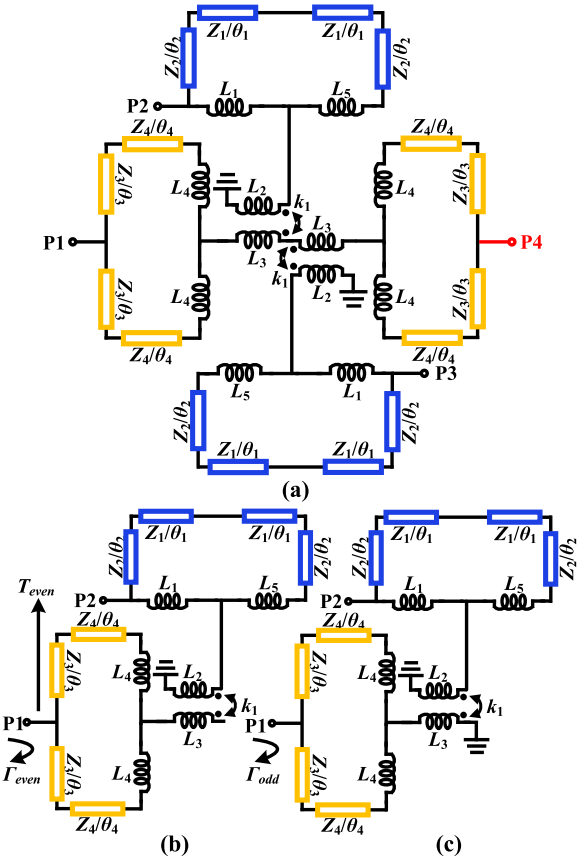

Fig. 21. (a) Equivalent circuit of the proposed filtering balun with an additional port P4. (c) Even-mode circuit. (d) Odd-mode circuit.

resonators according to the center frequency of the filter specifications according to Figs. 3(b) and 6(b). The second step is to obtain the parameters about coupling relationship of the resonators and feed-line according to specification of bandwidth and TZ. The desired bandwidth can be obtained by adjusting the value of coupling coefficient k_1, as shown in Fig. 16(b). The suitable loading strength can be obtained by adjusting the tapped position of feed-line, according to Fig. 16(c) and (d). Then, the desired location of TZ can be obtained by adjusting the value of C and k_2 about cross couplings, according to Fig. 17(c) and (d). The third step is to implement the layout of the filter according to the parameters of the equivalent circuits.

Based on the design procedure mentioned above, the third-order BPF is fabricated in a standard 40-nm CMOS technology, as displayed in Fig. 19(a). The simulated and measured results of the S-parameters are shown in Fig. 19(b). The center frequency of the BPF is 28 GHz with the 3-dB FBW of 47%. The minimum in-band insertion loss is 2.9 dB. The return loss is better than 15 dB in the simulated result. However, due to the deviation of the dielectric parameters between simulation and practical fabrication and the parasitic parameters of GSG pad, the measured return loss is worse than 10 dB. Meanwhile, the stopband is up to 170 GHz with a rejection level higher than 27 dB. The stopband $|S_{11}|$ is higher than -4 dB up to 155 GHz. In addition, the core circuit size of the BPF is 258×283 μm^2. A comparison of the on-chip millimeter-wave BPFs with the state-of-the-arts is shown in Table I, which reveals that the proposed filters have merits of low insertion loss, wide stopband with high rejection level, and wideband low radiation.

IV. Implementation and Analysis of Filtering Balun Using SIDGS Resonators

The proposed SIDGS resonators are also useful in filtering balun design. The balun is implemented by three stacked-coupled SIDGS resonators. The feed-lines are tapped to each resonator for the input and two unbalanced outputs. The configuration and simplified equivalent circuit of the balun are shown in Figs. 20 and 21, which are similar to the third-order BPF with an additional port. To demonstrate the principle of the filtering balun, an open-circuited terminal of the equivalent circuit is replaced by a load (i.e., P4) to form a fully symmetrical network, as shown in Fig. 21(a). Thus, the even- and odd-mode analyses can be used for calculation, as shown in Fig. 21(b) and (c), respectively. According to [45], $S_{21} = -S_{31}$ can be achieved when

$$\frac{T_{\text{even}}(1-\Gamma_{\text{odd}})}{2-\Gamma_{\text{even}}-\Gamma_{\text{odd}}} = 0 \tag{44}$$

Γ_{even} and Γ_{odd} are the input reflection coefficients of the even- and odd-mode circuits, respectively, and T_{even} denotes the transmission coefficient of the even-mode circuit. To obtain T_{even}, the input impedance Z_{ine} of the even-mode circuit in Fig. 21(c) can be derived as

$$Z_{\text{ine}} = Z_3\frac{Z_4 - Z_3\tan\theta_3\tan\theta_4}{jZ_3\tan\theta_4 + jZ_4\tan\theta_3} \tag{45}$$

Γ_{even} can be derived as

$$\Gamma_{\text{even}} = \frac{Z_{\text{ine}} - Z_0}{Z_{\text{ine}} + Z_0}. \tag{46}$$

Note that Z_{ine} is imaginary. Thus, $|\Gamma_{\text{even}}| = 1$ and $|T_{\text{even}}| = 0$, which satisfy the condition of $S_{21} = -S_{31}$ in (44).

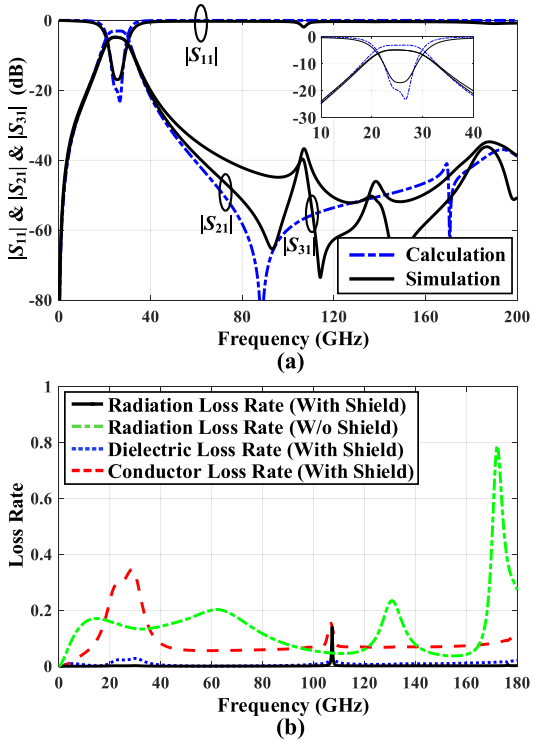

Fig. 22. (a) Calculated and simulated $|S_{11}|$, $|S_{21}|$, and $|S_{31}|$ of the filtering balun. (b) Simulated radiation/conductor/dielectric loss rates of the filtering balun ($l_1 = 246.6$, $l_2 = 19.62$, $l_3 = 293.76$, $l_4 = 120.15$, $l_5 = 246.6$, $l_6 = 42.3$, $l_7 = 198$, $l_8 = 142.92$, $l_9 = 44.55$, $l_{10} = 180.45$, $l_{11} = 21.42$, $d_1 = 5.4$, $d_2 = 1.8$, $d_3 = 1.8$, $d_4 = 5.4$, $d_5 = 3.6$, $w_1 = 2.16$, and $w_2 = 3.6$, unit: μm. $L_1 = 24$ pH, $L_2 = 141$ pH, $L_3 = 231$ pH, $L_4 = 30$ pH, $L_5 = 6$ pH, $k_1 = 0.36$, $Z_1 = 22\ \Omega$, $Z_2 = 25\ \Omega$, $Z_3 = 21\ \Omega$, $Z_4 = 24\ \Omega$, $\theta_1 = 21.1°$, $\theta_2 = 2.6°$, $\theta_3 = 12.5°$, and $\theta_4 = 1.3°$).

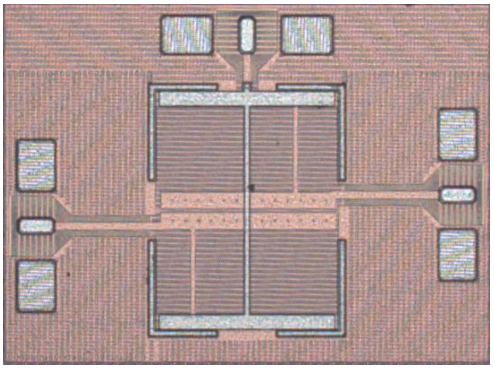

Fig. 23. Photograph of the filtering balun.

To calculate the frequency response of the balun, the input impedance Z_{ino} of the odd-mode circuit can be derived as (47), shown at the bottom of the page, from the circuit in Fig. 21(c),

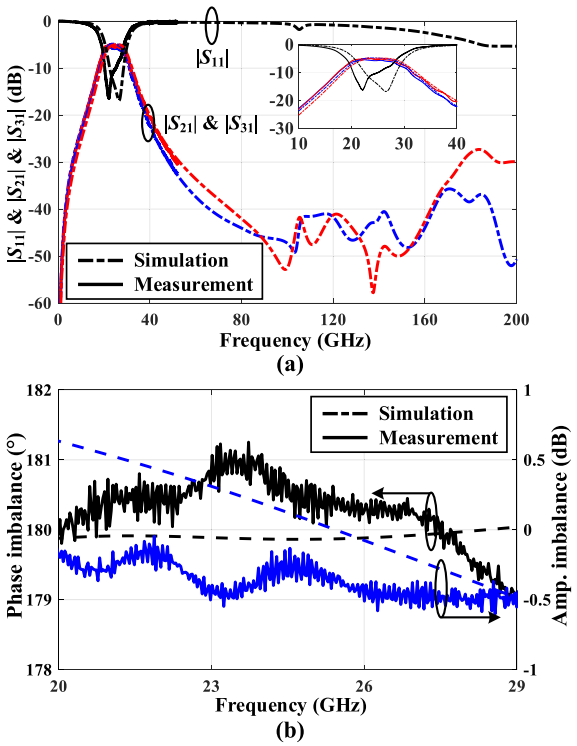

Fig. 24. Measured and simulated results of the proposed filtering balun. (a) S-parameters. (b) In-band amplitude and phase imbalances.

where Z_y is derived as

$$Z_y = j\omega(L_3 - M) - \frac{j\omega M(j\omega(L_2 - M) + Z_x)}{j\omega M + j\omega(L_2 - M) + Z_x}. \quad (48)$$

Z_x can be derived as

$$\frac{1}{Z_x} = Y_x = Y_{11} - \frac{Y_{12}Y_{21}}{Y_0 + Y_{22}} \quad (49)$$

where $Y_0 = 1/50$ S. Y_{11}, Y_{22}, Y_{12}, and Y_{21} are calculated as

$$Y_{11} = \frac{D_1}{B_1} + \frac{D_2}{B_2} \quad (50)$$

$$Y_{12} = \frac{B_1C_1 - A_1D_1}{B_1} + \frac{B_2C_2 - A_2D_2}{B_2} \quad (51)$$

$$Y_{21} = \frac{-1}{B_1} + \frac{-1}{B_2} \quad (52)$$

$$Y_{22} = \frac{A_1}{B_1} + \frac{A_2}{B_2}. \quad (53)$$

A_i, B_i, C_i, and D_i ($i = 1, 2$) can be derived as (54), shown at the bottom of the page, and (55).

$$\begin{pmatrix} A_2 & B_2 \\ C_2 & D_2 \end{pmatrix} = \begin{pmatrix} 1 & j\omega L_1 \\ 0 & 1 \end{pmatrix}. \quad (55)$$

$$Z_{\text{ino}} = \frac{Z_3}{2} \frac{Z_4\left(j\omega L_4 + 2Z_y + jZ_4\tan\theta_4\right) + jZ_3\tan\theta_3\left(Z_4 + j\left(j\omega L_4 + 2Z_y\right)\tan\theta_4\right)}{Z_3\left(Z_4 + j\left(j\omega L_4 + 2Z_y\right)\tan\theta_4\right) + jZ_4\left(j\omega L_4 + 2Z_y + jZ_4\tan\theta_4\right)} \quad (47)$$

$$\begin{pmatrix} A_1 & B_1 \\ C_1 & D_1 \end{pmatrix} = \begin{pmatrix} \cos\theta_2 & jZ_2\cos\theta_2 \\ jY_2\sin\theta_2 & \cos\theta_2 \end{pmatrix} \begin{pmatrix} \cos 2\theta_1 & jZ_1\cos 2\theta_1 \\ jY_1\sin 2\theta_1 & \cos 2\theta_1 \end{pmatrix} \begin{pmatrix} \cos\theta_2 & jZ_2\cos\theta_2 \\ jY_2\sin\theta_2 & \cos\theta_2 \end{pmatrix} \begin{pmatrix} 1 & j\omega L_5 \\ 0 & 1 \end{pmatrix} \quad (54)$$

TABLE II
COMPARISON OF THE STATE-OF-THE-ART ON-CHIP BALUN

Ref.	Technology & Structure	Filter Function	f_c (GHz)	Insertion Loss (dB)	FBW (%)	Amp.-Imbalance (dB) /Phase-Imbalance (°)	Stopband Rejection	Core Size
[24]	0.18-μm CMOS & CPW	No	43.5	2	110	<±1/<±4	N/A	0.07 mm^2
[28]	SiGe BiCMOS & CPW	No	50	2	40	<±0.2/<2.7	N/A	0.036 mm^2
[29]	0.18-μm CMOS & CPW	No	40	2.5	125	<1/<±5	N/A	0.231 mm^2
[30]	0.18-μm CMOS & Coupled-Line	No	33.1	2	88	<1.3/<2.5	N/A	0.043 mm^2
[31]	0.13-μm SiGe & SSCMS	No	17.5	0.7	125.7	<±1/<±1.65	N/A	0.054 mm^2
[33]	GaAs pHEMT & XFMR	Yes	5.5	2	27.3	<0.63/<±3.7	>20 dB up to 20 GHz ($3.6f_c$)	1 mm^2
[34]	0.18-μm CMOS & MS	Yes	24	2.2	16.7	<0.3/<5	>30 dB up to 60 GHz ($2.5f_c$)	0.236 mm^2
This work	**40-nm CMOS & SIDGS**	**Yes**	**25**	**2**	**32**	**<0.6/<±1.1**	**>30 dB up to 50 GHz***	**0.097 mm^2**

*: The stopband is limited by the measurement setup. The stopband in simulation is up to 175 GHz ($7f_c$) with the rejection level larger than 30 dB.

The S-parameters are calculated as

$$S_{11} = \frac{Z_{\text{ine}} + Z_{\text{ino}} - 2Z_0}{Z_{\text{ine}} + Z_{\text{ino}} + 2Z_0} \tag{56}$$

$$|S_{21}| = |S_{31}| = \sqrt{\frac{1 - |S_{11}|^2}{2}}. \tag{57}$$

Fig. 22(a) shows the S-parameters calculated from the equivalent circuit of the balun and simulated from the layout. Besides, radiation/conductor/dielectric loss rates of the balun are simulated and calculated, as shown in Fig. 22(b). Note that there is a radiation point at around 100 GHz. Such radiation can cause the deviation between the practical layout to the simplified equivalent model.

The filtering balun is fabricated in a standard 40-nm CMOS technology, as displayed in Fig. 23. The simulated and measured results of the S-parameters are shown in Fig. 24. The center frequency of the BPF is 25 GHz with the 3-dB FBW of 32%. The minimum in-band insertion loss is 2 dB excluding the theoretical 3-dB loss. The in-band amplitude and phase imbalances are 0.6 dB and ±1.1°, respectively. Meanwhile, the stopband is up to 175 GHz with a rejection level higher than 30 dB according to simulation. Limited by the setup of the measurement, the stopband of the balun over 50 GHz cannot be measured. In addition, the core circuit size of the balun is 273×355 μm^2. A comparison of the on-chip millimeter-wave filtering balun with the state-of-the-arts is shown in Table II, which reveals that the proposed balun has merits of low in-band amplitude/phase imbalance and wide stopband with high rejection level.

V. CONCLUSION

In this article, two types of millimeter-wave SIDGS resonators are proposed for filter and balun implementation on the 40-nm CMOS. Such SIDGS resonators are composed of DGS with grounded shield and surrounding metal vias, which not only exhibit wide stopband with low radiation loss but also be flexible to integrate with active circuits. Different coupling methods based on the proposed SIDGS resonators are used to design second-/third-order BPFs and filtering balun. To verify the principle, the proposed filters and balun are fabricated in a standard 40-nm CMOS technology. The narrowband second-order filter and wideband third-order filter have merits of low insertion loss, wide upper stopband with high rejection level, wideband low radiation loss, and good passband selectivity. The filtering balun shows merits of low in-band amplitude/phase imbalances and wide stopband with high rejection level.

APPENDIX

Z_{ij}, Z'_{ij}, and Z''_{ij} (i, j = 1, 2, 3, 4) in Section III-A are the Z-matrix parameters of the coupled line shown in Fig. 9, which are derived as [43]

$$Z_{11} = Z_{22} = Z_{33} = Z_{44} = \frac{-j}{2}(Z_{2e} + Z_{2o}) \cot\theta_1 \tag{58}$$

$$Z_{12} = Z_{21} = Z_{34} = Z_{43} = \frac{-j}{2}(Z_{2e} - Z_{2o}) \cot\theta_1 \tag{59}$$

$$Z_{13} = Z_{31} = Z_{24} = Z_{42} = \frac{-j}{2}(Z_{2e} - Z_{2o}) \csc\theta_1 \tag{60}$$

$$Z_{14} = Z_{41} = Z_{23} = Z_{32} = \frac{-j}{2}(Z_{2e} + Z_{2o}) \csc\theta_1 \tag{61}$$

$$Z'_{11} = Z'_{22} = Z'_{33} = Z'_{44} = \frac{-j}{2}(Z_{2e} + Z_{2o}) \cot\theta_2 \tag{62}$$

$$Z'_{12} = Z'_{21} = Z'_{34} = Z'_{43} = \frac{-j}{2}(Z_{2e} - Z_{2o}) \cot\theta_2 \tag{63}$$

$$Z'_{13} = Z'_{31} = Z'_{24} = Z'_{42} = \frac{-j}{2}(Z_{2e} - Z_{2o}) \csc\theta_2 \tag{64}$$

$$Z'_{14} = Z'_{41} = Z'_{23} = Z'_{32} = \frac{-j}{2}(Z_{2e} + Z_{2o}) \csc\theta_2 \tag{65}$$

$$Z''_{11} = Z''_{22} = Z''_{33} = Z''_{44} = \frac{-j}{2}(Z_{2e} + Z_{2o}) \cot(\theta_1 + \theta_2) \tag{66}$$

$$Z''_{12} = Z''_{21} = Z''_{34} = Z''_{43} = \frac{-j}{2}(Z_{2e} - Z_{2o}) \cot(\theta_1 + \theta_2) \tag{67}$$

$$Z''_{13} = Z''_{31} = Z''_{24} = Z''_{42} = \frac{-j}{2}(Z_{2e} - Z_{2o}) \csc(\theta_1 + \theta_2) \tag{68}$$

$$Z''_{14} = Z''_{41} = Z''_{23} = Z''_{32} = \frac{-j}{2}(Z_{2e} + Z_{2o}) \csc(\theta_1 + \theta_2). \tag{69}$$

The relationship between physical dimensions of the coupled line and Z_{2e}, Z_{2o} can be established using the method in [46] with EM simulation.

REFERENCES

[1] T. S. D. Cheung and J. R. Long, "Shielded passive devices for silicon-based monolithic microwave and millimeter-wave integrated circuits," *IEEE J. Solid-State Circuits*, vol. 41, no. 5, pp. 1183–1200, May 2006.

[2] J. R. Long, Y. Zhao, W. Wu, M. Spirito, L. Vera, and E. Gordon, "Passive circuit technologies for mm-wave wireless systems on silicon," *IEEE Trans. Circuits Syst. I, Reg. Papers*, vol. 59, no. 8, pp. 1680–1693, Aug. 2012.

[3] S. Sun, J. L. Shi, L. Zhu, S. C. Rustagi, and K. Mouthaan, "Millimeter-wave bandpass filters by standard 0.18-μm CMOS technology," *IEEE Electron Devices Lett.*, vol. 28, no. 3, pp. 220–222, Mar. 2007.

[4] M. Miao and C. Nguyen, "A novel multilayer aperture-coupled cavity resonator for millimeter-wave CMOS RFICs," *IEEE Trans. Microw. Theory Techn.*, vol. 55, no. 4, pp. 783–787, Apr. 2007.

[5] C.-Y. Hsu, C.-Y. Chen, and H.-R. Chuang, "A 60-GHz millimeter-wave bandpass filter using 0.18-μm CMOS technology," *IEEE Electron Device Lett.*, vol. 29, no. 3, pp. 246–248, Mar. 2008.

[6] L. Nan, K. Mouthaan, Y. Z. Xiong, J. Shi, S. C. Rustagi, and B. L. Ooi, "Design of 60- and 77-GHz narrow-bandpass filters in CMOS technology," *IEEE Trans. Circuits Syst. II, Exp. Briefs*, vol. 55, no. 8, pp. 738–742, Aug. 2008.

[7] S.-C. Chang et al., "Compact millimeter-wave CMOS bandpass filters using grounded pedestal stepped-impedance technique," *IEEE Trans. Microw. Theory Techn.*, vol. 58, no. 12, pp. 3850–3859, Dec. 2010.

[8] K. Ma, S. Mou, and K. S. Yeo, "Miniaturized 60-GHz on-chip multimode quasi-elliptical bandpass filter," *IEEE Electron. Devices Lett*, vol. 34, no. 8, pp. 945–947, Aug. 2013.

[9] N. Mahmoud, A. Barakat, A. B. Abdel-Rahman, A. Allam, and R. K. Pokharel, "Compact size on-chip 60 GHz H-shaped resonator BPF," *IEEE Microw. Wireless Compon. Lett.*, vol. 26, no. 9, pp. 681–683, Sep. 2016.

[10] A. S. El-Hameed, A. Barakat, A. B. Abdel-Rahman, A. Allam, and R. K. Pokharel, "Ultracompact 60-GHz CMOS BPF employing broadside-coupled open-loop resonators," *IEEE Microw. Wireless Compon. Lett.*, vol. 27, no. 9, pp. 818–820, Sep. 2017.

[11] C.-L. Yang, S.-Y. Shu, and Y.-C. Chiang, "Analysis and design of a chip filter with low insertion loss and two adjustable transmission zeros using 0.18-μm CMOS technology," *IEEE Trans. Microw. Theory Techn.*, vol. 58, no. 1, pp. 176–184, Jan. 2010.

[12] L.-K. Yeh, C.-Y. Chen, and H.-R. Chuang, "A millimeter-wave CPW CMOS on-chip bandpass filter using conductor-backed resonators," *IEEE Electron Device Lett.*, vol. 31, no. 5, pp. 399–401, May 2010.

[13] C.-L. Yang, S.-Y. Shu, and Y.-C. Chiang, "Design of a K-band chip filter with three tunable transmission zeros using a standard 0.13-μm CMOS technology," *IEEE Trans. Circuits Syst. II, Exp. Briefs*, vol. 57, no. 7, pp. 522–526, Jul. 2010.

[14] A.-L. Franc, E. Pistono, D. Gloria, and P. Ferrari, "High-performance shielded coplanar waveguides for the design of CMOS 60-GHz bandpass filters," *IEEE Trans. Electron Devices*, vol. 59, no. 5, pp. 1219–1226, May 2012.

[15] S. Chakraborty et al., "A broadside-coupled meander-line resonator in 0.13-μm SiGe technology for millimeter-wave application," *IEEE Electron Device Lett.*, vol. 37, no. 3, pp. 329–332, Mar. 2016.

[16] Y. Zhong, Y. Yang, X. Zhu, E. Dutkiewicz, K. M. Shum, and Q. Xue, "An on-chip bandpass filter using a broadside-coupled meander line resonator with a defected-ground structure," *IEEE Electron Device Lett.*, vol. 38, no. 5, pp. 626–629, May 2017.

[17] Y. Yang, H. Liu, Z. J. Hou, X. Zhu, E. Dutkiewcz, and Q. Xue, "Compact on-chip bandpass filter with improved in-band flatness and stopband attenuation in 0.13-μm (Bi)-CMOS technology," *IEEE Electron Device Lett.*, vol. 38, no. 10, pp. 1359–1362, Oct. 2017.

[18] H. Zhu, X. Zhu, Y. Yang, and Y. Sun, "Design of miniaturized on-chip bandpass filters using inverting-coupled inductors in (Bi)-CMOS technology," *IEEE Trans. Circuits Syst. I, Reg. Papers*, vol. 67, no. 2, pp. 647–657, Feb. 2020.

[19] M. G. Bautista, H. Zhu, X. Zhu, Y. Yang, Y. Sun, and E. Dutkiewicz, "Compact millimeter-wave bandpass filters using quasi-lumped elements in 0.13-μm (Bi)-CMOS technology for 5G wireless systems," *IEEE Trans. Microw. Theory Techn.*, vol. 67, no. 7, pp. 3064–3073, Jul. 2019.

[20] F. Sun, H. Zhu, X. Zhu, Y. Yang, and R. Gomez-Garcia, "Design of on-chip millimeter-wave bandpass filters using multilayer patterned-ground element in 0.13-μm (Bi)-CMOS technology," *IEEE Trans. Microw. Theory Techn.*, vol. 67, no. 12, pp. 5159–5170, Dec. 2019.

[21] H. Zhu, Y. Yang, X. Zhu, Y. Sun, and S.-W. Wong, "Miniaturized resonator and bandpass filter for silicon-based monolithic microwave and millimeter-wave integrated circuits," *IEEE Trans. Circuits Syst. I, Reg. Papers*, vol. 65, no. 12, pp. 4062–4071, Dec. 2018.

[22] H. Zhu, X. Zhu, Y. Yang, and Q. Xue, "Design of wideband third-order bandpass filters using broadside-coupled resonators in 0.13-μm (Bi)-CMOS technology," *IEEE Trans. Microw. Theory Techn.*, vol. 66, no. 12, pp. 5593–5604, Dec. 2018.

[23] F. Wang and H. Wang, "A broadband linear ultra-compact mm-wave power amplifier with distributed-balun output network: Analysis and design," *IEEE J. Solid-State Circuits*, vol. 56, no. 8, pp. 2308–2323, Aug. 2021.

[24] H. K. Chiou and J. Y. Lin, "Symmetric offset stack balun in standard 0.13-μm CMOS technology for three broadband and low-loss balanced passive mixer designs," *IEEE Trans. Microw. Theory Techn.*, vol. 59, no. 6, pp. 1529–1538, May 2011.

[25] I. Ju, C. D. Y. Cheon, and J. D. Cressler, "A compact highly efficient high-power Ka-band SiGe HBT cascode frequency doubler with four-way input transformer balun," *IEEE Trans. Microw. Theory Techn.*, vol. 66, no. 6, pp. 2879–2887, Jun. 2018.

[26] C.-S. Lin et al., "Analysis of multiconductor coupled-line Marchand baluns for miniature MMIC design," *IEEE Trans. Microw. Theory Techn.*, vol. 55, no. 6, pp. 1190–1199, Jun. 2007.

[27] H.-M. Hsu, J.-S. Huang, S.-Y. Chen, and S.-H. Lai, "Design of an on-chip balun with a minimum amplitude imbalance using a symmetric stack layout," *IEEE Trans. Microw. Theory Techn.*, vol. 58, no. 4, pp. 814–819, Apr. 2010.

[28] K. Ma, N. Yan, K. S. Yeo, and W. M. Lim, "Miniaturized 40–60 GHz on-chip balun with capacitive loading compensation," *IEEE Electron Device Lett.*, vol. 35, no. 4, pp. 434–436, Apr. 2014.

[29] Y.-C. Hsiao, C. Meng, and Y.-H. Peng, "Broadband CMOS Schottky-diode star mixer using coupled-CPW Marchand dual-baluns," *IEEE Microw. Wireless Compon. Lett.*, vol. 27, no. 5, pp. 500–502, May 2017.

[30] G. Yang, Z. Wang, Z. Li, Q. Li, and F. Liu, "Balance-compensated asymmetric Marchand baluns on silicon for MMICs," *IEEE Microw. Wireless Compon. Lett.*, vol. 24, no. 6, pp. 391–393, Jun. 2014.

[31] H. J. Qian and X. Luo, "Compact 6.5–28.5 GHz on-chip balun with enhanced inband balance responses," *IEEE Microw. Wireless Compon. Lett*, vol. 26, no. 12, pp. 993–995, Dec. 2016.

[32] Y.-S. Lin, C.-W. You, and C.-L. Tsai, "On-chip single-to-balanced multicoupled line bandpass filters with good selectivity," *IEEE Trans. Microw. Theory Techn.*, vol. 58, no. 4, pp. 814–819, Apr. 2010.

[33] C.-F. Chang and Y.-S. Lin, "On-chip transformer-coupled balun bandpass filter for 5-GHz applications," in *IEEE MTT-S Int. Microw. Symp. Dig.*, Phoenix, AZ, USA, May 2015, pp. 1–4.

[34] C.-W. You and Y.-S. Lin, "A 24-GHz single-to-balanced multicoupled line bandpass filter in CMOS technology," in *Proc. Asia–Pacific Microw. Conf.*, Kaoshiung, Taiwan, Dec. 2012, pp. 262–264.

[35] D. Tang, C. Han, Z. Deng, H. J. Qian, and X. Luo, "Substrate-integrated defected ground structure for single- and dual-band bandpass filters with wide stopband and low radiation loss," *IEEE Trans. Microw. Theory Techn.*, vol. 69, no. 1, pp. 659–670, Jan. 2021.

[36] C. Han, D. Tang, Z. Deng, H. J. Qian, and X. Luo, "Filtering power divider with ultrawide stopband and wideband low radiation loss using substrate integrated defected ground structure," *IEEE Microw. Wireless Compon. Lett.*, vol. 31, no. 1, pp. 113–115, Feb. 2021.

[37] D. Tang and X. Luo, "Compact filtering balun with wide stopband and low radiation loss using hybrid microstrip and substrate-integrated defected ground structure," *IEEE Microw. Wireless Compon. Lett.*, vol. 31, no. 6, pp. 549–552, Jun. 2021.

[38] J. Zhou, Y. Rao, D. Yang, H. J. Qian, and X. Luo, "Compact wideband BPF with wide stopband using substrate integrated defected ground structure," *IEEE Microw. Wireless Compon. Lett.*, vol. 31, no. 4, pp. 353–356, Apr. 2021.

[39] J. Xie, D. Tang, Y. Shu, and X. Luo, "Compact UWB BPF with broad stopband based on loaded-stub and C-shape SIDGS resonators," *IEEE Microw. Wireless Compon. Lett.*, vol. 32, no. 5, pp. 383–386, May 2022.

[40] R. Garg, I. Bahl, and M. Bozzi, *Microstrip Lines and Slotlines*, 3rd ed. Boston, MA, USA: Artech House, 2013.

[41] C.-C. Wang, H.-C. Chiu, and T.-G. Ma, "A slow-wave multilayer synthesized coplanar waveguide and its applications to rat-race coupler and dual-mode filter," *IEEE Trans. Microw. Theory Techn.*, vol. 59, no. 7, pp. 1719–1729, Jul. 2011.
[42] W. R. Eisenstadt and Y. Eo, "S-parameter-based IC interconnect transmission line characterization," *IEEE Trans. Compon., Hybrids, Manuf. Technol.*, vol. 15, no. 4, pp. 483–490, Apr. 1992.
[43] D. M. Pozar, *Microwave Engineering*, 4th ed. New York, NY, USA: Wiley, 2012.
[44] J. R. Long, "Monolithic transformers for silicon RF IC design," *IEEE J. Solid-State Circuits*, vol. 35, no. 9, pp. 1368–1382, Sep. 2000.
[45] K. S. Ang, Y. C. Leong, and C. H. Lee, "Analysis and design of miniaturized lumped-distributed impedance-transforming baluns," *IEEE Trans. Microw. Theory Techn.*, vol. 51, no. 3, pp. 1009–1017, Mar. 2003.
[46] D. Chowdhury, P. Reynaert, and A. M. Niknejad, "Design considerations for 60 GHz transformer-coupled CMOS power amplifiers," *IEEE J. Solid-State Circuits*, vol. 44, no. 10, pp. 2733–2744, Oct. 2009.

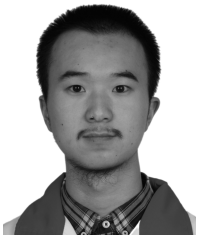

Deshan Tang (Graduate Student Member, IEEE) received the B.E. degree in information and communication engineering from the University of Electronic Science and Technology of China, Chengdu, China, in 2022, where he is currently pursuing the Ph.D. degree in microelectronics and solid-state electronics.

His research interests include reconfigurable RF/microwave filter and passive components.

Mr. Tang was a recipient of the 2021 IEEE MTT-Society Undergraduate/Pre-Graduate Scholarship Award.

Xun Luo (Senior Member, IEEE) received the B.E. and Ph.D. degrees in electronic engineering from the University of Electronic Science and Technology of China (UESTC), Chengdu, China, in 2005 and 2011, respectively.

From 2010 to 2013, he was with Huawei Technologies Company Ltd., Shenzhen, China, as the Project Manager to guide research and development projects of multiband microwave/millimeter-wave (mm-wave) integrated systems for backhaul and wireless communication. Before joining UESTC, he was an Assistant Professor with the Department of Microelectronics, Delft University of Technology, Delft, The Netherlands. Since 2015, he has been with UESTC as a Full Professor, where he has been appointed as the Executive Director of the Center for Integrated Circuits. Since 2020, he has also been the Head of the Center for Advanced Semiconductor and Integrated Micro-System (ASIS), UESTC. He has authored or coauthored more than 130 journals and conference papers. He holds 45 patents. His research interests include RF/microwave/mm-wave integrated circuits, multiple-resonance terahertz (THz) modules, multibands backhaul/wireless systems, reconfigurable passive circuits, smart antenna, and system in package.

Dr. Luo is a Technical Program Committee Member of multiple IEEE conferences, including the IEEE Radio Frequency Integrated Circuits (RFIC) Symposium and the IEEE Custom Integrated Circuits Conference (CICC). He is also the IEEE MTT-Society Technical Committee Member of MTT-4 on Microwave Passive Components and Transmission Line Structures, MTT-5 on Filters, and MTT-23 on Wireless Communications. He was bestowed by China with the China Overseas Chinese Contribution Award in 2016 and was selected by the IEEE MTT-Society for the IEEE Outstanding Young Engineer Award in 2022. He, along with the Center for ASIS, was a recipient of the UESTC Outstanding Team for Teaching and Education Award in 2021 and the UESTC Excellent Team for Postgraduate Supervision Award in 2021. He also received the UESTC Distinguished Innovation and Teaching Award in 2018 and the UESTC Outstanding Undergraduate Teaching Promotion Award in 2016. His Research Group BEAM X-Laboratory received multiple best paper awards and design competition awards, including the IEEE RFIT Best Student Paper Award in 2016 and 2019, the IEEE IWS Best Student Paper Award in 2015 and 2018, the IEEE IMS Student Design Competition Award from 2017 to 2019, the IEEE IMS Sixty-Second Presentation Competition Award in 2019, multiple best paper award finalists from the IEEE conferences, and the IEEE RFIC Best Student Paper Award in 2021. He was the TPC Co-Chair for the IEEE IWS in 2018 and the IEEE RFIT in 2019. He is the Vice-Chair for the IEEE MTT-Society Chengdu Chapter. He serves as an Associate Editor for *IET Microwaves, Antennas & Propagation*. He was the Track Editor of IEEE MICROWAVE AND WIRELESS COMPONENTS LETTERS from 2018 to 2021.